Honeycombs in Honeycombs: Complex Liquid Crystal Alumina Composite Mesostructures

Ruibin Zhang,[†] Xianbing Zeng,[†] Marko Prehm,[‡] Feng Liu,[†] Silko Grimm,[§,⊥] Markus Geuss,[§] Martin Steinhart,[§,⊥] Carsten Tschierske,[‡,*] and Goran Ungar[†,∥,*]

[†]Department of Materials Science and Engineering, University of Sheffield, Sheffield S1 3JD, United Kingdom, [‡]Institute of Chemistry, Martin-Luther-University Halle-Wittenberg, Kurt-Mothes-Strasse 2, D-06120 Halle, Germany, [§]Max Planck Institute of Microstructure Physics, Halle, Germany, [⊥]Institut für Chemie neuer Materialien, Universität Osnabrück, Barbarastrasse 7, D-49076 Osnabrück, and [∥]Department of Physics, Zhejiang Sci-Tech University, Xiasha College Park, Hangzhou 310018, China

ABSTRACT Small-angle X-ray scattering (SAXS) and atomic force microscopy (AFM) were used to study orientation patterns of two polyphilic liquid crystals (LC) confined to cylindrical pores of anodic aluminum oxide (AAO). The hierarchical hybrid systems had the LC honeycomb (lattice parameter 3.5−4 nm) inside the pores of the AAO honeycomb (diameters 60 and 400 nm). By conducting complete reciprocal space mapping using SAXS, we conclude that the columns of both compounds align in planes normal to the AAO pore axis, with a specific crystallographic direction of the LC lattice aligning strictly parallel to the pore axis. AFM of LC-containing AAO fracture surfaces further revealed that the columns of the planar anchoring LC (compound 1) formed concentric circles in the plane normal to the pore axis near the AAO wall. Toward the pore center, the circles become anisometric "racetrack" loops consisting of two straight segments and two semicircles. This mode compensates for slight ellipticity of the pore cross section. Indications are, however, that for perfectly circular pores, circular shape is maintained right to the center of the pore, the radius coming down to the size of a molecule. For the homeotropically anchoring compound 2, the columns are to the most part straight and parallel to each other, arranged in layers normal to the AAO pore axis, like logs in an ordered pile. Only near the pore wall the columns splay somewhat. In both cases, columns are confined to layers strictly perpendicular to the AAO pore axis, and there is no sign of escape to the third dimension or of axial orientation, the latter having been reported previously for some discotic LCs. The main cause of the two new LC configurations, the "racetrack" and the "logpile", and of their difference from those of confined nematic LC, is the very high splay energy and low bend energy of columnar phases.

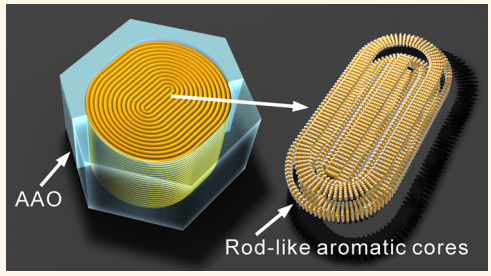

KEYWORDS: columnar liquid crystals · confinement · anodized alumina · AAO · AFM · atomic force · X-ray diffraction · SAXS · nanochannels · disclinations

The use of hard templates containing arrays of aligned cylindrical nanopores, such as self-ordered nanoporous anodic aluminum oxide (AAO),[1,2] has been exploited as a versatile access to one-dimensional nanoobjects.[3−5] Self-ordered AAO membranes feature narrow distribution of pore diameter and uniform pore depth. Since their hydroxyl-terminated pore walls have high surface energy,[6] liquid soft matter with low surface energy spontaneously infiltrates the AAO pores, enabling the creation of rod-like nanostructures and advanced membrane configurations. Nanoscopic domain structures of block copolymers (BCPs) formed in cylindrical confinement have been investigated theoretically[7−9] and experimentally. BCP melts predominantly self-assemble into bulk-like nanoscopic morphologies adapted to the curvature of the pore walls, if the pore diameter exceeds the period of the BCP several times.[10−12] In sol/gel systems containing cylinder-forming BCPs or surfactants as structure-directing agents with periods one to several orders of magnitude smaller than the pore diameter, there is subtle competition between the formation of straight cylinders parallel or perpendicular to the pore axis and circular cylinders oriented parallel to the pore walls.[13−16] If the pore diameter approaches the period of the BCP, nanoscopic morphologies substantially different from their bulk counterparts containing, for example, toroidal and helical structures form both in the case of BCP melts[17−20] and sol/gel systems containing BCPs.[21]

* Address correspondence to g.ungar@sheffield.ac.uk, carsten.tschierske@chemie.uni-halle.de.

Received for review December 20, 2013 and accepted April 23, 2014.

Published online April 23, 2014
10.1021/nn406368e

© 2014 American Chemical Society

The structural length scale of liquid crystals (LCs) is one to 2 orders of magnitude smaller than that of microphase-separated BCPs. Configuration of nematic[22−28] and smectic-A[29−32] LCs in cylindrical cavities has been studied in some detail, including a study of the nematic phase of discotic molecules.[33] Nanopatterning of complex morphologies, such as nanopillars of, *e.g.*, n-type semiconductors interdigitating a matrix of its counterpart p-type material, is a promising mode of building solar cells,[34,35] and if columnar LCs were to be used, their orientation within the pillars would be crucial. Large discotic molecules in the columnar LC phase have been shown to align with the columns parallel to the long axis of the nanocylinder cavities.[36−38] After removal of the AAO "molecular wires" were obtained in this way.[35] However, with smaller discs the column orientation within AAO pores or porous silicon is less clear and straightforward.[39,40]

Confined alignment of more complex LC superstructures is also of considerable interest, among them honeycomb LC phases consisting of triangular, square, hexagonal and other cylinder cells obtained in recent years with T- or X-shaped ternary amphiphiles.[41−46] These could serve, *e.g.*, as ionic channels or could themselves act as subtemplates for arranging small nanoparticles or individual molecules within the larger pores of the AAO template. Furthermore, because of the wide range of geometries of LC honeycombs from these amphiphiles, they are well placed to provide a broader understanding of the behavior of columnar LC under confinement.

Here we report on nanocomposites where fluid LC honeycombs with hexagonal and square geometries self-assemble inside AAO pores arranged in hexagonal arrays; *i.e.*, we study fluid honeycombs in solid honeycombs. Moreover, due to the segregation of the three incompatible units of the ternary polyphile (aromatic core, hydrogen bonding glycerol groups and nonpolar chains), the space inside the pores is divided into three different sets of compartments instead of only two as observed for the pores filled with BCPs or discotic LCs. The arrangement of the LC inside the AAO was determined by reconstructing three-dimensional X-ray diffraction patterns and mapping the whole low-q reciprocal space. This, combined with direct AFM imaging of crack surfaces, provides a unique insight into the internal molecular organization of confined soft structures in unprecedented detail.

RESULTS AND DISCUSSION

Results of X-ray Diffraction. The liquid crystal compounds used in this work are T-shaped ternary amphiphiles **1**[47] and **2**[48] shown in Figure 1. Both compounds form liquid crystalline phases over a wide temperature range from below room temperature to 91 and 161 °C, respectively. The facial amphiphile **1** forms a square honeycomb phase, where the rigid rod-like terphenyls

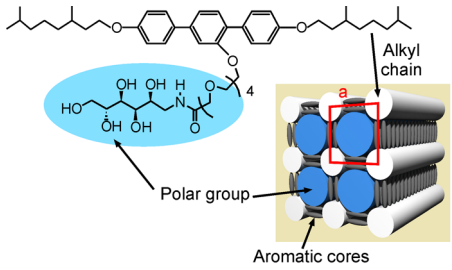

1: G -8 $Col_{squ}/p4mm$ 94 Iso; a_{squ} = 3.9 nm

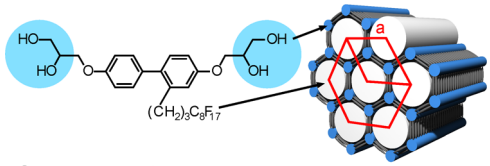

2: Cr <20 $Col_{hex}/p6mm$ 161 Iso; a_{hex} = 3.5 nm

Figure 1. Structures of the compounds investigated,[48] their phase types, transition temperatures, and lattice parameters as bulk materials and models showing the organization in their LC phases. Polar regions, blue; aliphatic, white; aromatic, dark gray.

(gray in Figure 1) make up the walls, the terminal alkyl chains form the cell edges (white columns), and the interior of the cells is filled with the polar lateral groups composed of a carbohydrate unit and an oligo(ethylene glycol) spacer (blue columns). On the other hand, the bolaamphiphile **2** has the positions of the hydrophilic and hydrophobic groups reversed with respect to the rigid core. It exhibits a hexagonal honeycomb where the biphenyl walls are connected at the edges by columns containing the hydrogen bonding networks of the glycerol terminal groups (blue columns); here the cells are filled with the semiperfluorinated laterally attached chains (white columns).

According to the DSC thermogram of AAO filled with compound **1**, the LC-isotropic transition temperature was no different from that of the bulk LC. The phase type was also unaffected by the confinement.

To determine the orientation of the honeycombs inside the AAO, a series of 2-D diffraction patterns were recorded of the AAO filled with each of the two compounds using synchrotron radiation (for details see Supporting Information). The AAO membranes were mounted and aligned vertically on a motorized goniometer and rotated about the vertical axis in increments of $\Delta\phi = 1°$ (see Figure 2a). Figures 2b,c show selected diffraction patterns from compounds **1** (Figure 2b) and **2** (Figure 2c) in AAO membranes with a pore diameter of 400 nm.

For both compounds, in the $\phi = 0°$ diffraction patterns (AAO pores parallel to beam) the strongest reflection is spread around a circle of uniform intensity (but see note in caption for Figure 2). For both compounds, the strongest is the (10) reflection of the 2-D lattice, square in compound **1** and hexagonal in compound **2**. As ϕ is increased, the intensity condenses on

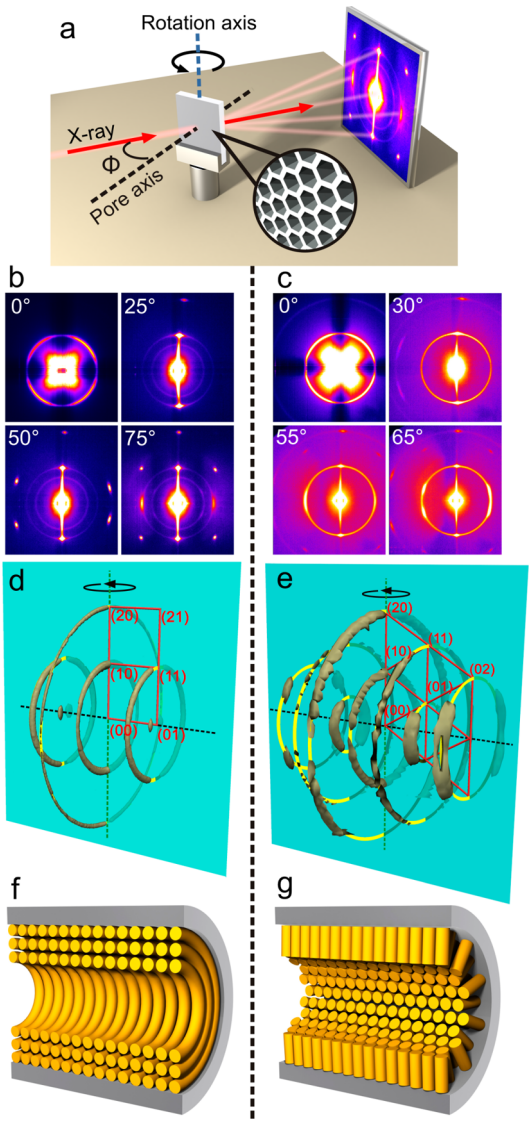

Figure 2. (a) The X-ray diffraction setup used, showing the LC-infiltrated AAO membrane on the goniometer irradiated by the X-ray beam, with the area detector at the back. The rotation angles ϕ is the angle between the beam and the membrane normal (*i.e.*, the AAO pore axis). (b and c) X-ray diffraction patterns of AAO membranes (pore diameter 400 nm) filled with LC compounds 1 (b) and 2 (c) recorded at a series of rotation angles ϕ indicated. Note that the four-quadrant sectorization in the $\phi = 0°$ patterns is an artifact due to the saturation of the detector with the intense central scatter from the AAO pores. (d and e) 3-D diffraction patterns of (d) compound 1 and (e) compound 2 confined to AAO with a pore diameter of 400 nm in reciprocal space coordinates. The isosurface is set to an intensity level such that the reciprocal space distribution of all three strongest reflection groups, *i.e.*, {10}, {11}, and {20}, could be shown simultaneously. The dashed black line indicates the orientation of the pores in the AAO. The continuous background scatter predominantly originating from AAO was subtracted by means of a custom-written 3-D fitting algorithm. The breaks in the rings are mainly due to absorption of X-rays by the AAO. They are most prominent in the plane containing the AAO pore axis and the axis of rotation (the blue semitransparent plane), as diffraction for $\phi = 90°$ is not accessible. The yellow lines are guides to the eye. (f and g) Two of the possible models of columns in cylindrical confinement that fit the X-ray data: (f) planar circular (for planar, or homogeneous surface anchoring) and (g) planar radial (for homeotropic anchoring); these models assume cylindrical D_∞ symmetry within each AAO pore.

the meridian (meridian and equator are defined here with respect to the rotation axis, *i.e.*, meridian is vertical, equator horizontal). However, as ϕ increases, in both compounds new reflections appear on the equator, then split and move away from it. For compound **1**, this happens when ϕ reaches 45° and then again around $\phi = 75°$; the latter reflection remains equatorial. These events mark the crossing of the Ewald sphere by the {11} reciprocal rings and the (01/0$\bar{1}$) reciprocal spots, respectively. The full reciprocal space map is shown in Figure 2d. The contour map shows a single-level isointensity surface chosen so as to capture the essence of the 3-d intensity distribution in reciprocal space.

The behavior of the diffraction pattern of compound **2** with increasing ϕ is similar to that of compound **1** taking account of the fact that the 2-D lattice of compound 2 is hexagonal rather than square. The complete reciprocal space map of the three strongest reflection groups {10}, {11}, and {20} for compound **2** is shown in Figure 2e. Here, the {10} reflection group is separated in three rings containing, respectively, (10$\bar{1}$)($\bar{1}$01), (01$\bar{1}$)(0$\bar{1}$1), and ($\bar{1}$10)(1$\bar{1}$0) reflections, using the three *hki* Miller indices of the 2-D hexagonal lattice.

Assuming cylindrical (D_∞) symmetry within each AAO pore, three special cases of columnar organization could be envisaged. These are (i) axial (columns parallel to AAO pore axis), (ii) planar radial (columns normal to pore walls; see Figure 2g), and (iii) planar circular (concentric circular columns in plane normal to pore axis; Figure 2f). The observed appearance of additional equatorial diffraction arcs at, respectively, around ϕ = 45° and 55° and their subsequent splitting into four arcs is *decidedly inconsistent with axial orientation* (case (i)). Had the columns of the honeycomb been parallel to the AAO pore axis, all Bragg diffraction intensity in Figure 2d would have been condensed in the reciprocal plane normal to the pore axis. In terms of the diffraction patterns, for all $\phi \neq 0$, all reflections would have been meridional, including (11) and (01). Instead, the 3-D diffraction pattern of both compounds **1** and **2** (Figure 2d,e) are consistent with the 2-D reciprocal net being rotationally averaged around a [10] axis, *i.e.*, an axis *in the plane* of the 2-D lattice rather than perpendicular to it. The patterns are actually consistent with both radial (case (ii)) and circular columnar arrangements (case (iii)). Other planar arrangements also become possible if one removes the condition of rotational symmetry within individual AAO pores, and allows the rotational symmetry of the diffraction pattern to be a result of averaging over all irradiated pores.

Notably, from the reciprocal space maps it also follows that the AAO pore axis (horizontal in Figure 2d,e) coincides with a defined low-index vector of the reciprocal lattice; in compound **1**, this is labeled (01), and in compound **2**, it is ($\bar{1}$2), equivalent to (11).

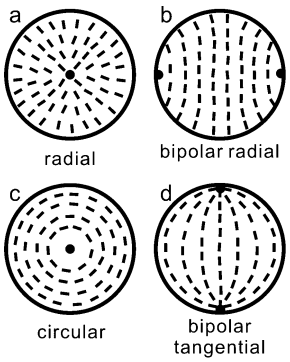

Figure 3. Planar director configurations of nematic LCs in cylindrical confinement. The director (dashed) is confined within the plane shown, normal to the pore axis.[26] The black spots indicate the defect line.[26]

Thus, not only are the columns perpendicular to the AAO pore axis, but so are the layers containing the columns. These layer are the {10} and {11} planes of the square and hexagonal lattices, respectively, in compounds **1** and **2**. Compared to nematics, the extra order parameter describing the in-plane orientation of the 2-D lattice adds a further dimension to the description of columnar LCs in nanoconfinement.

AAO templates with 60 nm pores, filled with compounds **1** and **2**, show very similar diffraction features as AAO templates with 400 nm pores, except for additional line broadening associated with reduced correlation length.

Thus, in both compounds the columns align in layers perpendicular to the pore axis. Unfortunately, both the radial and the circular configuration could produce the same rotational averaging of the reciprocal lattice, and we cannot distinguish between them solely on the basis of reciprocal space mapping. Furthermore, because the diffraction averages over the entire irradiated volume, on the basis of the evidence presented so far, we cannot ascertain whether cylindrical symmetry is the property of each individual AAO pore or the result of spatial averaging over many pores.

Studies on nematic LCs confined in cylindrical cavities have shown that their configurations are largely affected by their surface anchoring. The possible configurations for homeotropic anchoring (columns normal to surface) are radial, bipolar radial (sheaf-like), and escaped radial;[22,49] see Figure 3. The escaped radial features "escape in the 3rd dimension", *i.e.*, a nonplanar whirl-like center that serves to avoids high splay deformation. For planar anchoring, the director could adopt axial, circular, or bipolar tangential configuration.[22f,50] The latter has two line defects running along the pore walls diametrically across from each other, as in bipolar radial. However in the tangential case the two disclinations are negative, while in the radial bipolar, they are positive.

Polarized optical microscopy was done on compounds **1** and **2** deposited on flat glass and alumina substrates. These samples were treated by the same thermal procedure as that of the template samples in order to achieve the same anchoring condition. We used transmission microscopy on samples between glass slides (Figure S1 in Supporting Information), and reflection microscopy on samples on flat alumina. Compound **1** showed "spherulitic" texture typical of columnar LCs with planar alignment. In contrast, compound **2** exhibited a nonbirefringent dendritic texture, indicating homeotropic alignment of the LC columns. Incidentally, we believe that the reason compound **1** columns prefer to lie parallel to the substrate is that some polar side chains in the layer next to the substrate turn outward maximizing the contact with the polar surface. This option is not available to compound **2** that has nonpolar side chains. As our X-ray diffraction results exclude axial or any noticeable amount of "escaped" orientation, by analogy with nematics we may expect either circular or bipolar tangential configurations in compound **1**, and radial or bipolar radial in compound **2**; see Figure 3.

AFM of Confined Compound 1. To find out which, if any, of the above configurations are adopted by the honeycomb columns in our compounds, we performed AFM imaging on the LCs inside AAO templates. In principle, one can attempt to image the surface of the AAO membrane to observe the LC in the pores by allowing the tip to enter the pore. Figure 4a shows a relatively successful result of a number of such attempts; this one for AAO with 400 nm pores filled with compound **1**. One should recall that the entrance to an AAO pore is conical, the pore tapering down to its final diameter and becoming cylindrical only a few tens of nanometers below the surface, as visible in Figure 4a,c. The surface of the LC is sunk below the pore entrance, making it difficult to scan with high-resolution probes. Nevertheless, in favorable cases, such as in Figure 4a, one may see the organization of individual columns; see the high-resolution inset in Figure 4a. The image suggests that the columns tend to run parallel to the wall, although the configuration is rather complicated, with a bundle of columns "escaping" into the layer above, forming two screw dislocations, and finally hitting the wall homeotropically. The width of the narrow columns packed at the center is about 3.9 nm, which is consistent with the square lattice parameter calculated from SAXS. The outer wide bands are likely to be artifacts due to the stiff edge at the end of the pore where the probe could not reach the LC sample and was "scanned" by the edge instead.

The above method of AFM imaging is clearly not ideal: the AAO surface is not necessarily representative of the interior of the AAO pores as the pores are conically widened at their mouth. Moreover, scanning is difficult due to uneven surface. To observe the LC columns in the pore interior, we resorted to a fracture surface method. Infiltrated AAO was cracked open at

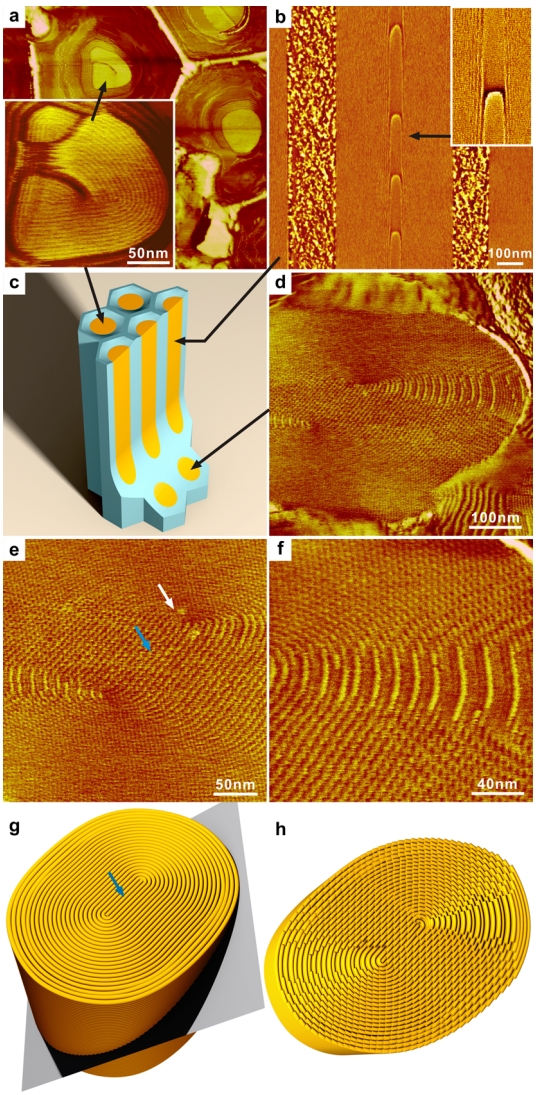

Figure 4. (a–f) AFM phase images obtained at different surfaces of AAO with 400 nm pores filled with compound 1: (a) top surface; (b) fracture surface parallel to AAO pore axis (inset shows a zoom-in of the central axis region); (c) schematic of the fractured part of the AAO membrane showing areas from where the different images were taken; (d) tilted-cut surface (in this case *ca.* 20 μm away from membrane surface); (e and f) higher resolution images from the area in (d). (g) Model of the interior of an AAO pore showing circular and "racetrack" LC columns; a tilted-cut plane is also shown; (h) same as (g) after removing the upper slice (compare with (d–f)).

room temperature, and the fracture surface was immediately scanned by AFM. Both compounds **1** and **2** were waxy solids at room temperature, and the variety and consistency of textures obtained for different fracture orientations shown below suggest strongly that these images represent the true state of the bulk LC interior and are not a result of surface reconstruction.

We first describe the observations on compound **1**, whose larger column width makes AFM observation easier. Individual LC columns were successfully observed at the fracture surface of the LC inside the AAO pores. We found that most of the fractures went through the membrane first parallel to the pores, then bent and intersected the pores at an angle, as schematically shown in Figure 4c (see also SEM images in Figure S3). This kind of crack was beneficial for our observation, as it exposed different sections through the confined LC. Figure 4b shows a groove created by the crack running almost exactly along the central axis of an AAO pore. The LC texture resembles that of a tree trunk cleaved along the middle. The timber-like texture with the "tree-rings" is clearer in the enlarged detail in the inset in Figure 4b. On the obliquely cracked surface, the AAO pores appear as elliptical holes (Figures 4d and S4, the projection of the tilted pore axis is horizontal). Within them, individual LC columns are seen clearly forming nearly circular loops following the AAO pore wall. The dark lines are likely to be the soft aliphatic regions, while the bright columns represent the hard aromatic regions. Note the sector to the right of the pore center that contains some "thick" columns. These are steps on the fracture plane that is tilted with respect to the plane of the circular columns. The situation is clearer in the higher resolution detail in Figure 4f, and is explained in the model in Figure 4h.

It is interesting to consider the configuration at the center of the AAO pores; see Figure 4e. There is one or, at most, two straight columns in the center (indicated by blue arrow in Figure 4e,g) surrounded by two column loops of increasing circumference, each loop consisting of two parallel straight segments joined at each end by a semicircle. This "racetrack"-shaped loops spread all the way virtually to the AAO wall, with the radius of the semicircles increasing and the length of the straight segments remaining approximately unchanged. In this way adjacent columns remain parallel everywhere, with virtually no splay. There are two disclinations of strength $+1/2$ at each end of the central straight column, one of them marked by white arrow in Figure 4e. It is remarkable that the radius of the semicircular part of the innermost loop is only 1.5×4 nm $= 6$ nm. That such a sharp U-turn is stable shows that the bend modulus of the columns within the (10) plane is very low.

To illustrate the high bendability of the honeycomb columns, in Figure 5 we show a very small droplet of compound **1** on flat mica surface (see the larger area image in Figure S5). Individual concentric circular columns are seen. The single layer of columns in this circular droplet is confined in a circular disk by the droplet surface. The arrangement corresponds to circular concentric arrangement in Figure 3c, a situation never actually observed in nematic LCs. Unlike in nematics, in the present case there is no escape in the third dimension, or vortex formation, or formation of bipolar texture; rather there is only one pure disclination of strength $+1$. Figure 5b displays a molecular model of the inner circular column marked by arrow in (a), giving an impression of column deformation on molecular scale.

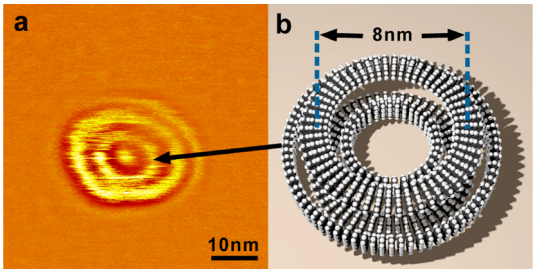

Figure 5. (a) AFM phase image of a small droplet of 1 on mica. Individual concentric circular columns are seen. The hard aromatic rod-like mesogens are bright, while the softer glycerol regions are dark. (b) Molecular model of one circular loop representing the column marked by arrow in (a), having a diameter of 8 nm. Only the terphenyl rod-like groups are shown, while the end and side chains are omitted for clarity.

The low bend modulus is in sharp contrast to the splay modulus, which is prohibitively high in columnar LCs. This low-bend/high-splay moduli combination is a feature of columnar phases, and is the very opposite of that of the nematic phase. The reason for the high splay energy of the columnar phases, including the current square honeycomb, is the need to insert new columns between the adjacent nonparallel columns, leaving large vacancies and many high-energy column ends, or dislocations. We propose that this difference between columnar and nematic LCs is the reason for the difference in configurations of the two classes of planar-anchored LCs in confinement, as illustrated by comparing Figures 3c,d and 4g.

We also propose that the particular column arrangement in the center of the AAO pore is the result of the fact that most pores are not perfectly circular but have a certain degree of ellipticity. AFM observation on the AAO pore in Figure 4 and on other pores suggests that the length of the straight portion of the column loops is determined by the difference between the long and the short axis of the elliptically distorted pore cross section (*cf.* Figure S4). However, rather than being elliptical themselves, the loops adopt the "racetrack" shape in order to minimize splay. The inevitable small amount of splay is thereby relegated to the region close to the pore wall, where the curvature and hence the required amount of splay are lowest. It is likely that the energy of small splay deformation is relatively low, as the deformation can be achieved by straining the square 2-D lattice rather than inserting new columns. However, it would appear that the "racetrack" configuration exists only because the pore cross section is not perfectly circular. If it was, the column loops would also be perfectly circular and, as in the case of the circular droplet in Figure 5, there would be no need to split the central +1 disclination into two +1/2 ones.

AFM of Confined Compound 2. Figure 6a shows the phase image of one AAO pore containing compound **2** that had been cut at a small angle to the pore axis. The width of this particular groove is 328 nm, indicating

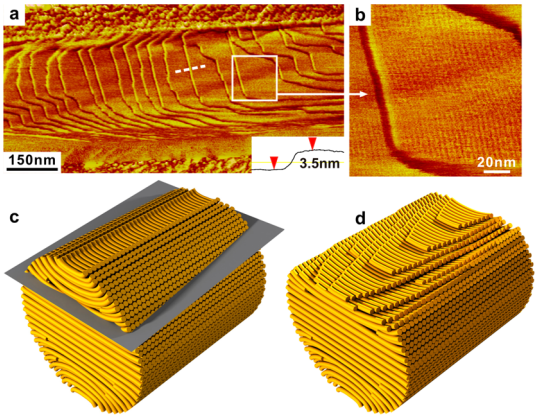

Figure 6. AFM phase images of a 400 nm diameter AAO pore filled with compound 2 and fractured nearly parallel to the pore axis. (a) Terrace-like structure of the LC; since the AAO groove is only 328 nm wide, the cut was off-center; inset is the height scan along the dashed white line. (b) High resolution phase image of the area marked by the white square in (a), showing individual columns parallel to the step and perpendicular to the AAO pore axis (Fourier filtered). (c) 3-D model of the "logpile" of columns cut by a plane slightly inclined to the pore axis. (d) As (c) but with the top slice removed.

that a 400 nm AAO pore was cut off-center. The terraces that are seen in this groove arise from the slightly oblique cut through layers of columns. The layers run parallel to the AAO pore axis, and in this particular pore, the layers are fortuitously also very nearly parallel to the fracture plane. The thickness of a layer is about 3.5 nm, as measured from the height profile scanned along the dashed white line in Figure 6a and shown in the inset. This compares reasonably well with the 3.0 nm spacing between (10) planes of the hexagonal lattice of compound **2**, confirming that the layers are one column thick. Furthermore, in the high-resolution image, individual LC columns are resolved within the layers (Figure 6b), and are seen to be oriented perpendicular to the AAO pore axis. The periodicity between the columns is about 3.5 nm, matching well the 3.5 nm *a*-parameter of the hexagonal unit cell. The columns are, thus, packed as straight logs in an ordered pile, perpendicular to the pore axis.

We should point out that in most other sections column-containing layers ((10) planes) are rotated about the pore axis away from the fracture plane, so that steps are encountered as one moves not only along the AAO pore axis, but also perpendicular to it, *i.e.*, along a column. This is exemplified in Figure 7a and explained on a 3-D model in Figure 7b,c. The latter observations also confirm that the arrangement of the LC columns is well preserved after fracture at room temperature, with little or no surface reconstruction during or after the fracture.

The features in Figure 6a,b are consistent with the model in Figure 6c,d. This model is somewhat related to the bipolar radial model in confined nematics

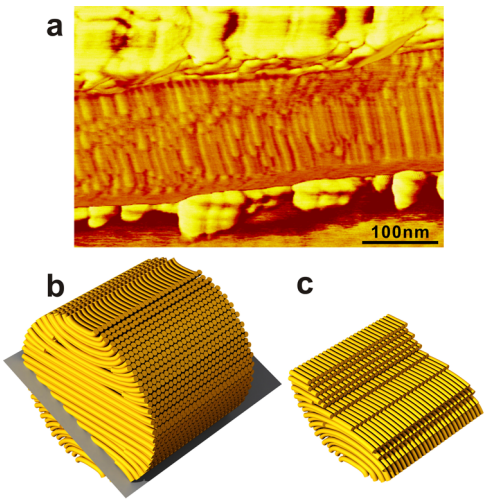

Figure 7. (a) AFM phase image of a typical AAO pore filled with compound 2 fractured along the pore axis. In this, as in most cases, the layers of columns are at an angle to the fracture surface; hence, the columns are truncated by the fracture plane. (b) Model of a section of the AAO pore cut by the fracture plane, and (c) same but with the top slice removed. Unlike in the model (c), in the experimental image (a) the columns are truncated at irregular positions.

(Figure 3b), but for two main differences. The first is the existence of a specific crystallographic orientation of the hexagonal columnar lattice, with a (11) plane normal to the AAO pore axis and a (10) plane parallel to it. Obviously no such preference is possible in a nematic. Second, the director in the columnar phase, *i.e.*, the trajectory of the columns, is largely straight rather than curved as in the nematics (Figure 3b). Although the layers are flat and the columns straight in Figure 6a,b, we note that the terraces are truncated with obliquely clipped-off corners. This we attribute to the presence of some splay and bend out of the layer plane near the AAO wall, which is required for achieving homeotropic anchoring. Thus, the fracture plane trims off the resulting "dog ears", as shown in Figure 6c, d. Again, as in the case of the "racetrack" texture in compound **1**, in the "logpile" configuration of compound **2** splay is limited only to the peripheral region near the AAO wall rather than being spread over the entire pore cross-section.

It remains for us to comment on the orientation of the 2-D lattices relative to the AAO pore axis. In compound **2**, why is a {11} plane of the hexagonal lattice always perpendicular, and one of the {10} planes always parallel to the pore axis (Figure 2e), while on a flat substrate, a homeotropically oriented columnar LC has no preferred in-plane orientation? We suspect that when the columnar phase starts homeotropically growing from the pore wall, the orientation of the 2-D lattice could be affected by how the hexagonal array of the columns in the initial layer tiles the curved surface. Indeed, the observed preferred orientation is consistent with the report by Irvine and co-workers[51] of tiling of the hexagonal lattice of positively charged poly(methyl methacrylate) particles on the curved oil-glycerol interfaces. They showed that on the barrel surface, the lattice orients with one of its (10) planes parallel to the axis of the barrel. An alternative interpretation of our observation, based on consideration of thermodynamic equilibrium rather than nucleation control, is that the modulus of splay and/or bend about the hexagonal [11] axis of the columnar lattice is lower than that about any other direction, hence it is the [11] direction that aligns along the pore axis. A similar question applies to compound **1** whose columns align parallel to the surface on a flat substrate and arrange in concentric circles when inside AAO pores: why is there such a strong preference for one of the principal axis ([01] in Figure 2d) to align parallel to the axis of AAO pores? Here the answer is more straightforward: preliminary grazing-incidence X-ray diffraction on a thin film of **1** on a flat silicon substrate showed a strong preference for {10} planes to lie parallel to the substrate. That given, and as long as the columns in the pores form circles in a plane normal to the pore axis, it is inevitable that one of the principal axes of the lattice will align along the axis of the AAO pore.

CONCLUSIONS

In summary, the first examples of ordered multicompartment structures based on polyphilic liquid crystals with periods in the nanometre range were produced in the straight cylindrical pores of AAO. Also for the first time, detailed configuration in a confined columnar LC is shown on the scale of individual molecular columns. On the basis of a combination of the complete reciprocal space mapping by SAXS and direct observation by fracture surface AFM, it was shown that, for the planar anchoring LC **1**, columns form concentric circles in the plane normal to AAO pore axis near the AAO wall. Further in, the circles morph into concentric "racetrack" loops, to end in a narrow bundle of straight columns, or even in a single column, of finite length. Their two ends each define a +1/2 strength disclination. Such a layer of columns is replicated along the pore producing two parallel disclination lines. Such configuration copes with a small departure of the AAO pore cross section from perfectly circular. Indications from the configuration in nanodroplets (Figure 5) are that, if the pores were perfectly circular, the highly flexible columns would be able to remain circular right to the very center, tolerating extremely high curvature. For the homeotropically anchoring honeycomb compound **2**, the columns are to the most part straight and parallel to each other, arranged in layers normal to the pore axis, as in an ordered logpile. Only near the pore wall do the columns splay so as to approach the AAO wall in a direction closer to the wall normal. Here, the cylindrical symmetry observed by SAXS is entirely due to space averaging over many AAO pores.

Both configurations may be related, albeit somewhat remotely, to those in confined nematic LCs; the "racetrack" configuration in **1** to the planar circular, and the "logpile" configuration in **2** to the radial bipolar. In both cases, columns are confined to layers strictly perpendicular to the AAO pore axis, and there is no sign of escape to the third dimension in the pore center and, even less, of axial orientation. Thus, the arrangements of the LC columns in the present systems are different from those previously reported for discotic columnar LCs in AAO pores, where it was concluded that the columns were predominantly parallel to the AAO pore axis.[4] The key feature believed to underpin the behavior observed in the present "honeycomb in honeycomb" systems is the very high splay energy of columnar phases, resulting in the strong tendency of adjacent columns to be strictly parallel. As high splay modulus is a common feature of columnar systems, the observed configurations are expected to be replicated in a number of other confined columnar LCs.

The arrangement found in the present thermotropic systems, particularly the "logpile" type, can help explain some of the observed structures of nanoporous ceramics templated in AAO membranes by hexagonal lyotropic solutions.[14−16]

METHODS

Sample Preparation. The AAO membranes containing 100 μm deep pores 60 or 400 nm in diameter were prepared according to procedures reported elsewhere.[1,2] They were infiltrated with compounds **1** and **2** in their isotropic liquid state (**1**, 110 °C; **2**, 180 °C). Material remaining on the surface was carefully removed. The aluminum substrate, which the AAO membrane had initially been attached to, was selectively etched away with a mixture of 1.7 g of $CuCl_2 \cdot H_2O$, 50 mL of concentrated HCl, and 50 mL of deionized water. Thus, free-standing AAO membranes containing the LC were obtained. Prior to all experiments (X-ray and AFM), filled AAO membranes were heated to above the isotropization temperature of the LC and cooled slowly (0.5 K min^{-1}), in order to erase any flow-induced alignment and establish an equilibrium organization.

Construction of the 3-D Diffraction Pattern. Each spot (x,z) on the diffraction image corresponds to a point (q_x,q_y,q_z) in the reciprocal space. If we take the x' and z' axes in the q-space to be parallel to the x and z axes of the diffraction image, respectively, and y' axis as the direction of the incident beam, it can be shown that

$$q_{x'} = \frac{2\pi}{\lambda}\frac{x}{\sqrt{SD^2 + x^2 + z^2}}$$

$$q_{y'} = \frac{2\pi}{\lambda}\left(\frac{SD}{\sqrt{SD^2 + x^2 + z^2}} - 1\right)$$

$$q_{z'} = \frac{2\pi}{\lambda}\frac{z}{\sqrt{SD^2 + x^2 + z^2}}$$

Here SD is the sample to detector distance, and λ is the X-ray wavelength.

As the AAO membranes are rotated by ϕ, the axis of the reciprocal space is rotated by ϕ as well. Here the x and z axes are parallel to the AAO membrane, while the y axis is perpendicular to it, and we have

$$q_x = q_{x'}\cos\phi + q_{y'}\sin\phi$$

$$q_y = -q_{x'}\sin\phi + q_{y'}\cos\phi$$

$$q_z = q_{z'}$$

From the above equations, each spot on the diffraction images can be mapped onto the reciprocal space.

To construct the 3-D diffraction pattern, a cubic volume in the reciprocal space $(-Q < q_x,q_y,q_z < Q)$ is divided into typically 100 × 100 × 100 boxes. For each sample, every point of all diffraction images is then mapped to one of these boxes, and an averaged intensity value is taken for all the points that fall within a given box. The 3-D diffraction pattern is then examined in ParaView (Kitware, Inc.) using iso-intensity surfaces.

Microscopy Observation. Tapping mode AFM imaging was performed at room temperature on a Veeco Multimode instrument with Nanoscope IIIa controller. An Olympus BX-50 transmitted-light polarizing microscope equipped with a Mettler FP82 hotstage and a Coolsnap-Pro digital camera was used to observe the texture of the LCs. A Nikon Eclipse ME600 microscope in reflection mode was also used in this study.

Conflict of Interest: The authors declare no competing financial interest.

Acknowledgment. Financial support from the government of Saxonia-Anhalt through the Cluster of Excellence "Nanostructured Materials", DFG (FG 1145), and the PIRE RENEW project jointly financed by NSF and EPSRC (EP-K034308) are gratefully acknowledged. G.U. also acknowledges support from the Foreign Experts Program of the Government of China. We thank Prof. J. K. Hobbs for helpful advice on AFM, and Prof. N. Terrill and Dr. C. Pizzey at beamline I22, Diamond Light Source, for technical help, as well as K. Sklarek and S. Kallaus for the preparation of AAO.

Supporting Information Available: Details of SAXS experiments, optical micrographs, SAXS patterns of compounds in AAO pores of 60 nm diameter, SEM images of the cracked AAO template, additional AFM images of AAO pores filled with **2** and of nanodroplets of **1**. This material is available free of charge *via* the Internet at http://pubs.acs.org.

REFERENCES AND NOTES

1. Masuda, H.; Fukuda, K. Ordered Metal Nanohole Arrays Made by a Two-Step Replication of Honeycomb Structures of Anodic Alumina. *Science* **1995**, *268*, 1466–1468.
2. Masuda, H.; Yada, K.; Osaka, A. Self-Ordering of Cell Configuration of Anodic Porous Alumina with Large-Size Pores in Phosphoric Acid Solution. *Jpn. J. Appl. Phys., Part 2* **1998**, *37*, L1340–L1342.
3. Martin, C. R. Nanomaterials: A Membrane-Based Synthetic Approach. *Science* **1994**, *266*, 1961–1966.
4. Steinhart, M.; Wehrspohn, R. B.; Gösele, U.; Wendorff, J. H. Nanotubes by Template Wetting: A Modular Assembly System. *Angew. Chem., Int. Ed.* **2004**, *43*, 1334–1344.
5. Steinhart, M. Supramolecular Organization of Polymeric Materials in Nanoporous Hard Templates. *Adv. Polym. Sci.* **2008**, *220*, 123–187.
6. Fox, H. W.; Hare, E. F.; Zisman, W. A. Wetting Properties of Organic Liquids on High-Energy Surfaces. *J. Phys. Chem.* **1955**, *59*, 1097–1106.
7. He, X.; Song, M.; Liang, H.; Pan, C. Self-assembly of the Symmetric Diblock Copolymer in a Confined State: Monte Carlo Simulation. *J. Chem. Phys.* **2001**, *114*, 10510–10513.

8. Sevink, G. J. A.; Zvelindovsky, A. V.; Fraaije, J. G. E. M.; Huinink, H. P. Morphology of Symmetric Block Copolymer in a Cylindrical Pore. *J. Chem. Phys.* **2001**, *115*, 8226–8230.
9. Yu, B.; Sun, P. C.; Chen, T. C.; Jin, Q. H.; Ding, D. T.; Li, B. H.; Shi, A. C. Confinement-Induced Novel Morphologies of Block Copolymers. *Phys. Rev. Lett.* **2006**, *96*, 138306.
10. Xiang, H.; Shin, K.; Kim, T.; Moon, S. I.; McCarthy, T. J.; Russell, T. P. Block Copolymers Under Cylindrical Confinement. *Macromolecules* **2004**, *37*, 5660–5664.
11. Sun, Y. M.; Steinhart, M.; Zschech, D.; Adhikari, R.; Michler, G. H.; Gösele, U. Diameter-Dependence of the Morphology of PS-b-PMMA Nanorods Confined Within Ordered Porous Alumina Templates. *Macromol. Rapid Commun.* **2005**, *26*, 369–375.
12. Xu, Y.; Li, W.; Qiu, F.; Yang, Y.; Shi, A. C. Self-Assembly of ABC Star Triblock Copolymers under a Cylindrical Confinement. *J. Phys. Chem. B* **2009**, *113*, 11153–11159.
13. Liang, Z. J.; Susha, A. S. Mesostructured Silica Tubes and Rods by Templating Porous Membranes. *Chem.—Eur. J.* **2004**, *10*, 4910–4914.
14. Platschek, B.; Köhn, R.; Döblinger, M.; Bein, T. *In Situ* GISAXS Study of the Formation of Mesostructured Phases within the Pores of Anodic Alumina Membranes. *Langmuir* **2008**, *24*, 5018–5023.
15. Platschek, B.; Petkov, N.; Bein, T. Tuning the Structure and Orientation of Hexagonally Ordered Mesoporous Channels in Anodic Alumina Membrane Hosts: A 2D Small-Angle X-ray Scattering Study. *Angew. Chem., Int. Ed.* **2006**, *45*, 1134–1138.
16. Lee, K. J.; Min, S. H.; Jang, J. Mesoporous Nanofibers from Dual Structure-Directing Agents in AAO: Mesostructural Control and Their Catalytic Applications. *Chem.—Eur. J.* **2009**, *15*, 2491–2495.
17. Xiang, H.; Shin, K.; Kim, T.; Moon, S. I.; McCarthy, T. J.; Russell, T. P. From Cylinders to Helices upon Confinement. *Macromolecules* **2005**, *38*, 1055–56.
18. Shin, K.; Xiang, H. Q.; Moon, S. I.; Kim, T.; McCarthy, T. J.; Russell, T. P. Curving and Frustrating Flatland. *Science* **2004**, *306*, 76–76.
19. Xiang, H.; Shin, K.; Kim, T.; Moon, S.; McCarthy, T. J.; Russell, T. P. The Influence of Confinement and Curvature on the Morphology of Block Copolymers. *J. Polym. Sci., Part B: Polym. Phys.* **2005**, *43*, 3377–3383.
20. Dobriyal, P.; Xiang, H.; Kazuyuki, M.; Chen, J. T.; Jinnai, H.; Russell, T. P. Cylindrically Confined Diblock Copolymers. *Macromolecules* **2009**, *42*, 9082–9088.
21. Wu, Y. Y.; Cheng, G. S.; Katsov, K.; Sides, S. W.; Wang, J. F.; Tang, J.; Fredrickson, G. H.; Moskovits, M.; Stucky, G. D. Composite Mesostructures by Nano-confinement. *Nat. Mater.* **2004**, *3*, 816–822.
22. de Gennes, P. G. *The Physics of Liquid Crystals*; Clarendon: Oxford, 1974.
23. Allender, D. W.; Crawford, G. P.; Doane, J. W. Determination of the Liquid-Crystal Surface Elastic Constant K_{24}. *Phys. Rev. Lett.* **1991**, *67*, 1442–1445.
24. Crawford, G. P.; Allender, D. W.; Doane, J. W. Finite Molecular Anchoring in the Escaped-Radial Nematic Configuration: A ^{2}H-NMR study. *Phys. Rev. A* **1991**, *44*, 2570–2577.
25. Crawford, G. P.; Vilfan, M.; Doane, J. W. Escaped-Radial Nematic Configuration in Submicrometer-Size Cylindrical Cavities: Deuterium Nuclear-Magnetic-Resonance Study. *Phys. Rev. A* **1991**, *43*, 835–842.
26. Crawford, G. P.; Allender, D. W.; Doane, J. W. Surface Elastic and Molecular-Anchoring Properties of Nematic Liquid Crystals Confined to Cylindrical Cavities. *Phys. Rev. A* **1992**, *45*, 8693–8708.
27. Ondris-Crawford, R. J.; Crawford, G. P.; Zumer, S.; Doane, J. W. Curvature-Induced Configuration Transition in Confined Nematic Liquid Crystals. *Phys. Rev. Lett.* **1993**, *70*, 194–197.
28. Ondris-Crawford, R. J.; Ambrozic, M.; Doane, J. W.; Zumer, S. Pitch-Induced Transition of Chiral Nematic Liquid Crystals in Submicrometer Cylindrical Cavities. *Phys. Rev. E* **1994**, *50*, 4773–4779.
29. Crawford, G. P.; Steele, L. M.; Ondris-Crawford, R. J.; Iannacchione, G. S.; Yeager, C. J.; Doane, J. W.; Finotello, D. Characterization of the Cylindrical Cavities of Anopore and Nucleopore Membranes. *J. Chem. Phys.* **1992**, *96*, 7788–7796.
30. Crawford, G. P.; Stannarius, R.; Doane, J. W. Surface-Induced Orientational Order in the Isotropic-Phase of a Liquid Crystal Material. *Phys. Rev. A* **1991**, *44*, 2558–2569.
31. Crawford, G. P.; Ondris-Crawford, R. J.; Doane, J. W.; Zumer, S. Systematic Study of Orientational Wetting and Anchoring at a Liquid-Crystal-Surfactant Interface. *Phys. Rev. E* **1996**, *53*, 3647–3661.
32. Jin, T.; Zalar, B.; Lebar, A.; Vilfan, M.; Zumer, S.; Finotello, D. Anchoring and Structural Transitions as a Function of Molecular Length in Confined Liquid Crystals. *Eur. Phys. J. E* **2005**, *16*, 159–165.
33. Jian, K. J.; Shim, H. S.; Schwartzman, A.; Crawford, G. P.; Hurt, R. H. Orthogonal Carbon Nanofibers by Template-Mediated Assembly of Discotic Mesophase Pitch. *Adv. Mater.* **2003**, *15*, 164–167.
34. Kim, D. H.; Lee, Y. H.; Lee, D. U.; Kim, T. W.; Kim, S.; Kim, S. W. Significant Enhancement of the Power Conversion Efficiency for Organic Photovoltaic Cells due to a P3HT Pillar Layer Containing ZnSe Quantum Dots. *Opt. Express* **2012**, *20*, 10476–10483.
35. Hu, J. C.; Shirai, Y.; Han, L. Y.; Wakayama, Y. Template Method for Fabricating Interdigitate p-n Heterojunction for Organic Solar Cell. *Nanoscale Res. Lett.* **2012**, *7*, 1–5.
36. Pisula, W.; Kastler, M.; Wasserfallen, D.; Davies, R. J.; Garcia-Gutierrez, M. C.; Müllen, K. *J. Am. Chem. Soc.* **2006**, *128*, 14424–14425.
37. Kastler, M.; Pisula, W.; Davies, R. J.; Gorelik, T.; Kolb, U.; Müllen, K. Nanostructuring with a Crosslinkable Discotic Material. *Small* **2007**, *3*, 1438–1444.
38. Duran, H.; Hartmann-Azanza, B.; Steinhart, M.; Gehrig, D.; Laquai, F.; Feng, X. L.; Mullen, K.; Butt, H. J.; Floudas, G. Arrays of Aligned Supramolecular Wires by Macroscopic Orientation of Columnar Discotic Mesophases. *ACS Nano* **2012**, *6*, 9359–9365.
39. Steinhart, M.; Zimmermann, S.; Göring, P.; Schaper, A. K.; Gösele, U.; Weder, C.; Wendorff, J. H. Liquid Crystalline Nanowires in Porous Alumina: Geometric Confinement *versus* Influence of Pore Walls. *Nano Lett.* **2005**, *5*, 429–434.
40. Cerclier, C. V.; Ndao, M.; Busselez, R.; Lefort, R.; Grelet, E.; Huber, P.; Kityk, A. V.; Noirez, L.; Schonhals, A.; Morineau, D. Structure and Phase Behavior of a Discotic Columnar Liquid Crystal Confined in Nanochannels. *J. Phys. Chem. C* **2012**, *116*, 18990–18998.
41. Tschierske, C. Liquid Crystal Engineering—New Complex Mesophase Structures and Their Relations to Polymer Morphologies, Nanoscale Patterning and Crystal Engineering. *Chem. Soc. Rev.* **2007**, *36*, 1930–1970.
42. Kölbel, M.; Beyersdorff, T.; Cheng, X. H.; Tschierske, C.; Kain, J.; Diele, S. Design of Liquid Crystalline Block Molecules with Nonconventional Mesophase Morphologies: Calamitic Bolaamphiphiles with Lateral Alkyl Chains. *J. Am. Chem. Soc.* **2001**, *123*, 6809–6818.
43. Cheng, X. H.; Das, M. K.; Baumeister, U.; Diele, S.; Tschierske, C. Liquid Crystalline Bolaamphiphiles with Semiperfluorinated Lateral Chains: Competition Between Layerlike and Honeycomb-like Organization. *J. Am. Chem. Soc.* **2004**, *126*, 12930–12940.
44. Prehm, M.; Liu, F.; Zeng, X. B.; Ungar, G.; Tschierske, C. The Giant-Hexagon Cylinder Network—A Liquid-Crystalline Organization Formed by a T-Shaped Quaternary Amphiphile. *Angew. Chem., Int. Ed.* **2007**, *46*, 7972–7975.
45. Prehm, M.; Götz, G.; Bäuerle, P.; Liu, F.; Ungar, G.; Tschierske, C. Complex Liquid-Crystalline Superstructure of a Pi-Conjugated Oligothiophene. *Angew. Chem., Int. Ed.* **2007**, *46*, 7856–7859.
46. Glettner, B.; Liu, F.; Zeng, X. B.; Prehm, M.; Baumeister, U.; Walker, M.; Bates, M. A.; Boesecke, P.; Ungar, G.; Tschierske, C. Liquid-Crystalline Kagome. *Angew. Chem., Int. Ed.* **2008**, *47*, 9063–9066.
47. Chen, B.; Baumeister, U.; Pelzl, G.; Das, M. K.; Zeng, X. B.; Ungar, G.; Tschierske, C. Carbohydrate Rod Conjugates:

Ternary Rod-Coil Molecules Forming Complex Liquid Crystal Structures. *J. Am. Chem. Soc.* **2005**, *127*, 16578–1659.
48. Cheng, X. H.; Prehm, M.; Das, M. K.; Kain, J.; Baumeister, U.; Diele, S.; Leine, D.; Blume, A.; Tschierske, C. Calamitic Bolaamphiphiles with (semi)Perfluorinated Lateral Chains: Polyphilic Block Molecules with New Liquid Crystalline Phase Structures. *J. Am. Chem. Soc.* **2003**, *125*, 10977–10996.
49. Cladis, P. E.; Kleman, M. Non-Singular Disclinations of Strength S = +1 in Nematics. *J. Phys. (Paris)* **1972**, *33*, 591–598.
50. Ondris-Crawford, R. J.; Ambrozic, M.; Doane, J. W.; Zumer, S. Pitch-Induced Transition of Chiral Nematic Liquid Crystals in Submicrometer Cylindrical Cavities. *Phys . Rev. E* **1994**, *50*, 4773–4779.
51. Irvine, W.; Vitelli, V.; Chaikin, P. Pleats in Crystals on Curved Surfaces. *Nature* **2010**, *468*, 947–951.